Topologically nontrivial magnons at an interface of two kagome ferromagnets

Alexander Mook,[1] Jürgen Henk,[2] and Ingrid Mertig[1,2]
[1]*Max-Planck-Institut für Mikrostrukturphysik, D-06120 Halle (Saale), Germany*
[2]*Institut für Physik, Martin-Luther-Universität Halle-Wittenberg, D-06099 Halle (Saale), Germany*
(Received 16 January 2015; revised manuscript received 2 April 2015; published 8 June 2015)

Magnon band structures of topological magnon insulators exhibit a nontrivial topology due to the Dzyaloshinskii-Moriya interaction, which manifests itself by topologically protected edge magnons. Bringing two topological magnon insulators into contact can lead to nontrivial unidirectional magnons located at their common interface. We study theoretically interfaces of semi-infinite kagome ferromagnets in various topological phases, with a focus on the formation and the confinement of nontrivial interface magnons. We analyze generic magnon dispersions with respect to the number of band gaps and the respective winding numbers. Eventually, we prove that interfaces of topologically identical phases can host nontrivial interface magnons as well.

DOI: 10.1103/PhysRevB.91.224411 PACS number(s): 66.70.−f, 75.30.−m, 75.47.−m, 85.75.−d

I. INTRODUCTION

For electrons, the spin-orbit interaction can induce band inversions and thus can yield nonzero topological invariants [1–3]. The bulk-boundary correspondence [4,5] relates these invariants of the bulk and the topological edge states that are protected by symmetry. The concepts of Berry curvature [6] and Chern numbers have entered various contexts and laws of condensed-matter physics. Topological arguments, first applied to electronic systems [7], have been carried forward, for instance, to phonons [8–10] as well as to magnons [11–13].

The application of topological concepts to magnons was initiated in large part by the discovery of the magnon Hall effect, that is, a transverse heat current upon application of a longitudinal temperature gradient [14]. This effect is explained by uncompensated magnon edge currents, and the thermal Hall conductivity can be expressed in terms of a Berry curvature [11,12]. The edge currents are associated with topological edge states owing to the nontrivial topology of the magnon band structure in "topological magnon insulators" (TMIs) [13]. As for electrons, the nontrivial topology is caused by the spin-orbit interaction which manifests itself as Dzyaloshinskii-Moriya interaction [15,16]. It shows up in systems that lack inversion symmetry, for example, in a pyrochlore lattice or in its two-dimensional counterpart, the kagome lattice [17].

The magnon Hall effect in kagome lattices is intimately related to topological edge states; if a TMI provides edge magnons all propagating in one and the same direction, the sign of the thermal Hall conductivity is unique within the entire topological phase to which the TMI belongs [18,19]. This finding is associated with the edges of the sample which may be viewed as interfaces to vacuum. The latter immediately suggests examining the formation of topological interface magnons at an interface of two TMIs, a "territory" unexplored to our knowledge.

In the present theoretical paper we report on such interface magnon formations at the junction of two semi-infinite commensurate and ferromagnetic kagome lattices. It turns out that energy-resolved winding numbers are a versatile tool for visualizing the bulk-boundary correspondence at the interface. We moreover analyze the decay of the interface states in the direction toward the bulk regions. Due to the rich topological phase diagram of the kagome TMIs one can construct a sizable number of interface magnon dispersions which differ with respect to the number of interface band gaps and topological states. On top of this we address the formation of nontrivial interface magnons between topologically identical phases.

This paper is organized as follows. In Sec. II we sketch the quantum-mechanical description of magnons in kagome lattices, Berry curvature, and the Chern number (Sec. II A) and the bulk-boundary correspondence and the Green's function renormalization method for calculating interface magnons in semi-infinite systems (Sec. II B). Results are presented in Sec. III: energy-resolved winding numbers dictating the number of interface states (Sec. III A), the confinement of nontrivial interface magnons (Sec. III B), and generic interface magnon dispersions (Sec. III C). An outlook is given in Sec. IV.

II. THEORY

A. Ferromagnetic kagome lattice: Model Hamiltonian and Chern number

The quantum-mechanical description of magnons in a ferromagnet is based on the Heisenberg model [20] with the Hamiltonian

$$\begin{aligned}\mathcal{H} &= \mathcal{H}_{\mathrm{iso}} + \mathcal{H}_{\mathrm{DM}} \\ &= -\sum_{m\neq n}\left[J_m^n \hat{\boldsymbol{s}}_m\cdot\hat{\boldsymbol{s}}_n - \boldsymbol{D}_m^n\cdot(\hat{\boldsymbol{s}}_m\times\hat{\boldsymbol{s}}_n)\right].\end{aligned} \tag{1}$$

Two spin operators $\hat{\boldsymbol{s}}_m$ and $\hat{\boldsymbol{s}}_n$, at sites m and n, respectively, are coupled by the isotropic symmetric Heisenberg exchange ($J_m^n = J_n^m$) and the antisymmetric Dzyaloshinskii-Moriya (DM) interaction ($\boldsymbol{D}_m^n = -\boldsymbol{D}_n^m$; Refs. [15,16]). For completeness, one could introduce the coupling of the spins to an external magnetic field or the anisotropic symmetric exchange. However, these contributions are irrelevant for our purpose.

The eigenstates of $\mathcal{H}_{\mathrm{iso}}$ are collective one-magnon excitations of spin 1 ($\hbar \equiv 1$). They read

$$|\boldsymbol{k}\rangle = \frac{1}{\sqrt{N}}\sum_m e^{i\boldsymbol{k}\cdot\boldsymbol{R}_m}|\boldsymbol{R}_m\rangle, \tag{2}$$

where $|\boldsymbol{R}_m\rangle$ denotes a state with all spins aligned with the maximum z component, except that at site m, whose z component

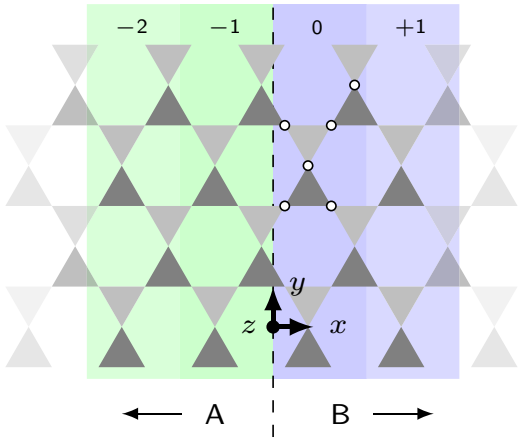

FIG. 1. (Color online) Sketch of facing semi-infinite kagome phases A (left, green) and B (right, blue), which share a common interface (dashed line) along the y direction. Each phase is divided into the thinnest principal layers possible (green and blue layers, respectively) if only nearest and next-nearest interactions are present in the Hamiltonian; four atomic layers form one principal layer from which four are numbered (on the top; $-2,\ldots,+1$). The six white dots in B indicate the principle-layer basis.

is reduced by 1. The solution of Eq. (1) in terms of one-magnon states is an approximation in which magnon-magnon interactions are neglected; it corresponds to keeping only bilinear terms in the infinite series of bosonic creation and annihilation operators, achieved by the Holstein-Primakoff transformation [21]. This "linear spin-wave theory" is valid at low temperatures, for which only a few magnons are excited [22].

The Dzyaloshinskii-Moriya interaction is nonzero in lattices that lack inversion symmetry. A two-dimensional kagome lattice meets this requirement; it consists of a three-atomic basis forming equilateral and corner-sharing triangles (Fig. 1). According to Moriya's symmetry rules [16], the DM vectors $\boldsymbol{D}_m^n$ are perpendicular to the kagome lattice, that is, $\boldsymbol{D}_m^n = D_m^n\,\hat{\boldsymbol{z}}$. The sign of D_m^n depends on the chirality of the triangles: it is positive (negative) for counterclockwise (clockwise) chirality.

Moriya's symmetry rules allow for an in-plane component of the DM vectors in a kagome system if and only if the kagome plane is not a mirror plane of the crystal, as is the case in jarosites [23]. Furthermore, pseudokagome ferromagnets or ferrimagnets that consist of buckled kagome layers allow for more complicated DM vectors; examples are the $Cu_3Bi(SeO_3)_2O_2X$ (X = Br, Cl, I) family [24,25] and the staircase kagome ferromagnet $Co_3V_2O_8$ [26]. These systems can be described by our strictly two-dimensional model with two approximations: (i) the buckled kagome lattice has to be projected onto the plane, resulting in a distorted in-plane geometry, and (ii) a magnetic field perpendicular to the kagome plane has to ensure a ferromagnetic ground state. The consequences of this magnetic field are twofold; it not only causes a uniform energy shift of the magnon band structure due to the Zeeman energy but also renders in-plane DM components irrelevant up to quadratic order in the spin deviation [14].

Because of the DM interaction a magnon accumulates an additional phase ϕ_m^n upon propagation from site m to n (see the supplemental online material in Ref. [14]). This becomes evident when using a representation of Eq. (1) in terms of ladder operators $\hat{s}^{\pm} = \hat{s}^x \pm i\hat{s}^y$,

$$\mathcal{H} = -\sum_{m\neq n}\left[\frac{\tilde{J}_m^n}{2}\left(e^{i\phi_m^n}\hat{s}_m^-\hat{s}_n^+ + e^{-i\phi_m^n}\hat{s}_m^+\hat{s}_n^-\right) + J_m^n\hat{s}_m^z\hat{s}_n^z\right], \quad (3)$$

with $\tilde{J}_m^n\exp(i\phi_m^n) = J_m^n + iD_m^n$. The eigenfunctions of $\mathcal{H}$ in Eq. (3) are again the one-magnon states defined in Eq. (2). The DM interaction can be viewed as introducing a vector potential which causes a textured flux within the plaquettes of the kagome lattice [27], in analogy to the Haldane model for an electronic topological insulator [28]. Thus, the DM interaction lifts crossings in the magnon dispersion, and one is concerned with a nonzero Berry curvature [6]

$$\boldsymbol{\Omega}_j(\boldsymbol{k}) \equiv i\sum_{i\neq j}\frac{\langle i(\boldsymbol{k})|\nabla_{\boldsymbol{k}}\mathcal{H}(\boldsymbol{k})|j(\boldsymbol{k})\rangle\times\langle j(\boldsymbol{k})|\nabla_{\boldsymbol{k}}\mathcal{H}(\boldsymbol{k})|i(\boldsymbol{k})\rangle}{[\varepsilon_i(\boldsymbol{k})-\varepsilon_j(\boldsymbol{k})]^2}, \quad (4)$$

which is aligned along $\hat{\boldsymbol{z}}$, $\boldsymbol{\Omega}_j(\boldsymbol{k}) = \Omega_j^z(\boldsymbol{k})\,\hat{\boldsymbol{z}}$, that is, perpendicular to the kagome plane. The Berry curvature is calculated from the eigenvectors $|i(\boldsymbol{k})\rangle$ and the corresponding eigenenergies $\varepsilon_i(\boldsymbol{k})$ [wave vector $\boldsymbol{k} = (k_x,k_y)$, band index i] of the 3×3 Hamilton matrix which is constructed from the Hamiltonian in Eq. (3). Its k derivative $\nabla_{\boldsymbol{k}}\mathcal{H}(\boldsymbol{k})$ is performed analytically. Thus, for a given set of exchange parameters $\{J_m^n, D_m^n\}$, we not only can calculate the magnon dispersion but also have access to its topology: the Brillouin zone (BZ) integral over the Berry curvature,

$$C_j \equiv \frac{1}{2\pi}\int_{\mathrm{BZ}}\Omega_j^z(\boldsymbol{k})\,dk^2, \quad (5)$$

defines the integer Chern number C_j of the jth bulk magnon band ($j = 1,2,3$). The sum $\sum_j C_j$ of all Chern numbers equals zero.

The evaluation of the integral in Eq. (5) can become complicated if two bands get very close, with the result that the Berry curvature becomes very large [see the denominator of Eq. (4)]. For certain parameters $\{J_m^n, D_m^n\}$ there are even degeneracies of the otherwise nondegenerate ferromagnetic magnon branches. In this case, the band gap closes, the Berry curvature diverges, and the Chern number is not defined. This set of parameters defines the topological phase boundaries. For nondegenerate magnon dispersions, we evaluate the Chern numbers by applying Gaussian integration on a 200×200 $\boldsymbol{k}$ mesh, which yields results with an accuracy better than 10^{-5}.

B. Winding numbers and nontrivial interface magnons

The Chern numbers C_j allow us to infer the nontrivial edge modes of a system, i.e., the bulk-boundary correspondence [1,4,5]. The winding number

$$\nu_i^{\mathsf{A}} \equiv \sum_{j\leqslant i} C_j^{\mathsf{A}} \quad (6)$$

of a material in topological phase A determines the number, $|\nu_i|$, and the propagation direction, $\mathrm{sgn}(\nu_i)$, of nontrivial edge magnons within the ith band gap.

The bulk-boundary correspondence holds for interfaces as well. For phases A and B sharing a common interface (Fig. 1),

the winding number of mutual interface band gaps is given by

$$\nu_l^{\mathsf{I}} = \nu_m^{\mathsf{A}} - \nu_n^{\mathsf{B}}, \tag{7}$$

where m and n denote those band gaps of A and B, respectively, that form the lth mutual interface band gap. This definition is fully in line with that given in Ref. [29]. The interface winding numbers determine the number and propagation direction of topological interface magnons.

To investigate interface magnons we consider two semi-infinite solids, A and B, sharing an interface along the y direction (Fig. 1). The magnon band structure is analyzed in terms of the spectral density which is computed by a Green's function renormalization technique [30,31] and is now briefly sketched. The facing semi-infinite crystals are decomposed into principal layers for which the exchange interaction is only among adjacent principal layers. For interactions restricted to nearest and next-nearest neighbors the thinnest principal layers are shown in Fig. 1. The resulting Hamilton matrix is block tridiagonal in the principal-layer indices. By means of the iterative renormalization process the effective interlayer interactions converge to zero, and the principal-layer-resolved Green's function blocks $G_{nm}(\varepsilon + i\eta, k_y)$ are obtained for given energy ε and parallel momentum k_y; the indices $-\infty < n,m < \infty$ denote the principal layers. The principal-layer-resolved spectral densities are obtained from the blocks G_{nn},

$$N_n(\varepsilon, k_y) = -\frac{1}{\pi} \lim_{\eta \to 0^+} \mathrm{Im\,tr}\; G_{nn}(\varepsilon + i\eta, k_y). \tag{8}$$

The limit $\eta \to 0^+$ is not taken, but $\eta = 0.0005$ meV. All G_{nm} can be computed from the interface block G_{00} by transfer matrices. This highly efficient approach avoids any finite-size effects that may occur in slab calculations [32].

III. RESULTS AND DISCUSSION

For the following we assume that both phases, A and B, share a common ideal kagome lattice. The basis atoms within each phase are identical, implying identical spins (here, $s = \frac{1}{2}$) and exchange parameters. That is, phase A has a unique set of exchange parameters which consists of nearest-neighbor exchange J_{N}, next-nearest-neighbor exchange J_{NN}, and nearest-neighbor Dzyaloshinskii-Moriya interaction D. The same holds for B but with a different set of exchange parameters. The explicit choice of the parameter sets is given in the captions of the figures showing calculated magnon dispersions. The exchange parameters of the interface equal the arithmetic mean of those of A and B.

The rich topological phase diagram of ferromagnetic kagome lattices has been extensively studied in Refs. [18,19]. Four topologically different phases were found with respect to the ratios $\frac{J_{\mathrm{NN}}}{J_{\mathrm{N}}}$ and $\frac{D}{J_{\mathrm{N}}}$ (Fig. 2). Each phase is uniquely characterized by its triple of Chern numbers $C = (C_1, C_2, C_3)$ and the corresponding winding numbers $\nu = (\nu_1, \nu_2)$ [see the definitions in Eqs. (5) and (6), respectively].

To construct an interface we choose two kagome phases with different ratios $\frac{J_{\mathrm{NN}}}{J_{\mathrm{N}}}$ and $\frac{D}{J_{\mathrm{N}}}$; that is, they are located at different points within the topological phase diagram but not necessarily within different topological phases.

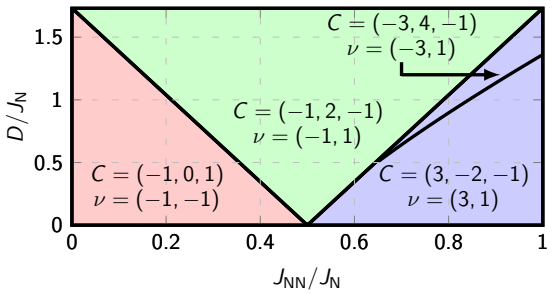

FIG. 2. (Color online) Topological phase diagram of ferromagnetic kagome lattices with respect to the ratios $\frac{J_{\mathrm{NN}}}{J_{\mathrm{N}}}$ and $\frac{D}{J_{\mathrm{N}}}$. The tinted topological phases are identified by their Chern numbers $C = (C_1, C_2, C_3)$ and winding numbers $\nu = (\nu_1, \nu_2)$.

A. Energy-resolved winding numbers

Being bosons, all magnons contribute to currents at a finite temperature. Hence, *all* gaps of the band structure have to be considered for the bulk-boundary correspondence which is conveniently visualized by energy-resolved winding numbers

$$\nu^{\mathsf{P}}(\varepsilon) = \frac{1}{2\pi} \sum_n \int_{\mathrm{BZ}} \Omega^z_{n,\mathsf{P}}(\boldsymbol{k})\, \Theta[\varepsilon - \varepsilon_{n,\mathsf{P}}(\boldsymbol{k})] dk^2, \tag{9}$$

where $\mathsf{P} = \mathsf{A},\mathsf{B}$; $\Theta(x)$ denotes the Heaviside step function. $\nu^{\mathsf{P}}(\varepsilon)$ is an integer within the band gaps of A or B. Thus, the energy-resolved interface winding number

$$\nu^{\mathsf{I}}(\varepsilon) \equiv \nu^{\mathsf{A}}(\varepsilon) - \nu^{\mathsf{B}}(\varepsilon) \tag{10}$$

is an integer within the *common* band gaps of A and B. It dictates the number and propagation direction of the nontrivial interface magnons in the considered band gap.

A positive (negative) winding number indicates propagation in the positive (negative) y direction for a sample which occupies the left-hand half space, for example, A in Fig. 1; the opposite holds for a sample occupying the right-hand half space, that is, B in Fig. 1. This property is evident from Figs. 3(a) and 3(c). Here, both A and B occupy the left-hand half space, while the right-hand half space is vacuum.

The energy-resolved winding number $\nu^{\mathsf{A}}(\varepsilon)$ for A with Chern triple $(-1,2,-1)$ starts from zero at $\varepsilon = 0$ [black line in Fig. 3(a)] and then decreases to -1 within the energy range of the lowest bulk band. Subsequently, it rapidly increases to $+1$ within the rather flat second bulk band. Eventually, it drops to zero above the uppermost bulk band. In general, $\nu^{\mathsf{A}}(\varepsilon)$ takes noninteger values within the energy range of the bulk bands, which is not relevant within this study. However, within the gaps it is integer and represents the number and the slope of the edge states, as is obvious from the spectral density for this A/vacuum interface. $\nu^{\mathsf{B}}(\varepsilon)$ for the B/vacuum interface exhibits a similar evolution; see Fig. 3(c) for B with Chern triple $(-1,0,1)$. Because the winding number is not inverted when passing the second band gap, both edge magnons traverse in the same direction (negative slope), which is different from phase A [Fig. 3(a)].

Before discussing the A/B interface, we recall that the spectral density and winding number of a vacuum/B interface can be obtained from those of the B/vacuum interface by vertically flipping Fig. 3(c), that is, by turning $k_y \to -k_y$

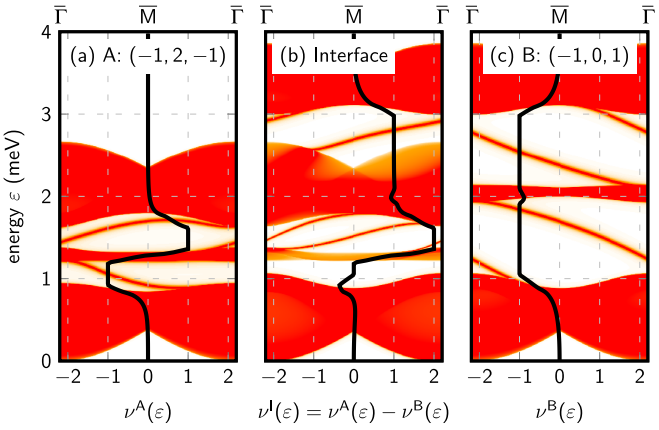

FIG. 3. (Color online) Bulk-boundary correspondence and energy-resolved winding numbers. (a) and (c) display energy-resolved winding numbers $\nu^{\mathsf{A}}(\varepsilon)$ and $\nu^{\mathsf{B}}(\varepsilon)$ (black lines) for an A/vacuum and a B/vacuum interface, respectively. These are superimposed on the spectral density of the rightmost principle layer (color scale, with white indicating zero spectral weight and dark orange indicating maximum weight). (b) shows the same quantities as (a) and (c) but for an A/B interface. Phase A with Chern triple $(-1,2,-1)$: $J_{\mathrm{N}} = {}^{23}\!/_{20} D = {}^{23}\!/_{10} J_{\mathrm{NN}} = 0.46\,\mathrm{meV}$; phase B with Chern triple $(-1,0,1)$: $J_{\mathrm{N}} = 2D = 1\,\mathrm{meV}$, $J_{\mathrm{NN}} = 0\,\mathrm{meV}$.

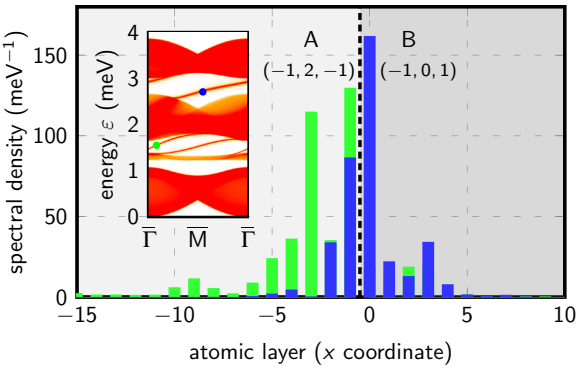

FIG. 4. (Color online) Localization of topological magnons at an A/B interface. The site-resolved spectral density is shown vs layer index for two interface magnons (blue and green histogram). The respective (ε, k_y) is marked by the blue (green) dot in the inset, which reproduces Fig. 3(b). Parameters are as in Fig. 3.

(not shown here). The spectral density of the A/B interface, depicted in Fig. 3(b), exhibits three band gaps since the second bulk band of A is located within the lower band gap of B; the upper bulk band of B tops the entire magnon dispersion of A. As a consequence, there is no topological interface magnon within the lowest band gap, according to $\nu_1^{\mathsf{I}} = \nu_1^{\mathsf{A}} - \nu_1^{\mathsf{B}} = (-1) - (-1) = 0$. For the second interface band gap, one has to subtract the first winding number of phase B from the second winding number of phase A, $\nu_2^{\mathsf{I}} = \nu_2^{\mathsf{A}} - \nu_1^{\mathsf{B}} = (1) - (-1) = +2$; hence, there are two topological interface magnons with positive dispersion. The winding number of the third interface band gap reads $\nu_3^{\mathsf{I}} = -\nu_2^{\mathsf{B}} = -(-1) = +1$, as the winding number of A equals zero at these energies. In total there are three ($|-2-1| = 3$) nontrivial interface magnons, all with positive velocity.

B. Localization of topological interface states

The confinement of topological edge magnons has been studied in Refs. [13,19]: the probability amplitude of edge magnons drops to zero within approximately ten atomic layers, confining them strongly to the sample edges. In the following, the localization of interface magnons is analyzed and compared to those of the associated edge magnons, utilizing the same systems as for Fig. 3.

We focus on two interface magnons and pick out representative (ε, k_y), specified by the green and blue dots in the inset of Fig. 4. The spectral densities are maximal at the interface layer but drop rapidly toward both bulk regions (green and blue histograms), that is, in both the $+x$ and $-x$ directions. Hence, the interface magnons are confined to a narrow strip, less than 20 atomic layers wide, around the interface. Their localization is close to that of the respective topological edge magnons (at an interface with vacuum, edge magnons cannot "spill over" into the vacuum, in contrast to magnons at an A/B interface). For a lattice constant a of 7.024 Å, associated with the vanadium sublattice of $Lu_2V_2O_7$ (Ref. [14]), the confinement width is less than 4 nm (the spacing of atomic layers parallel to the interface is $\frac{a}{4}$ for the geometry in Fig. 1). Being topologically protected, these modes follow unconditionally any geometry of the interface, e. g., corners.

C. Analysis of generic interface magnon dispersions

The exemplary interface dispersion relation shown in Fig. 3 foreshadows the variety of different interface band structures with respect to the energy positions of the band gaps of phases A and B. The two band structures of phases A and B, each with N bands and Chern numbers C_i^{A} and C_i^{B} $(i = 1, \ldots, N)$, respectively, produce $N-1$ winding numbers ν_j^{A} and ν_j^{B} $(j = 1, \ldots, N-1)$. Depending on the exchange parameters, the number of gaps at the interface can range from zero up to $M = 2(N-1)$. The lower limit $M = 0$ is obtained if the bulk bands of A match energetically the band gaps of B and vice versa; the upper limit $M = 2(N-1)$ requires the bulk bands of one phase to fit into the band gaps of the other phase, thereby, "splitting" these band gaps. We recall that the lowest bands of A and B have a common minimum energy because of the Goldstone modes; this is in contrast to interfaces of fermion band structures in which the Fermi levels of A and B coincide.

For ferromagnetic kagome lattices there are $N = 3$ bands and at most $M = 4$ band gaps at the interface. With respect to the number of interface gaps, there are various types of interface band structures. In the following we address three of them in detail (Fig. 5). The examples given on the right-hand side of Fig. 5 show not only the decay of the interface magnons toward the bulk regions but also the decay of the bulk magnons within the half space of the other phase. The color scales in these figures were chosen for clarity and do not allow a quantitative comparison, particularly with the results shown in Fig. 4.

For the interface dispersion shown in Fig. 5(a), all bulk bands of phase A match those of phase B, resulting in two interface winding numbers $\nu_i^{\mathsf{I}} = \nu_i^{\mathsf{A}} - \nu_i^{\mathsf{B}}$, $i = 1,2$. Hence, there are no topological interface magnons if A and B belong

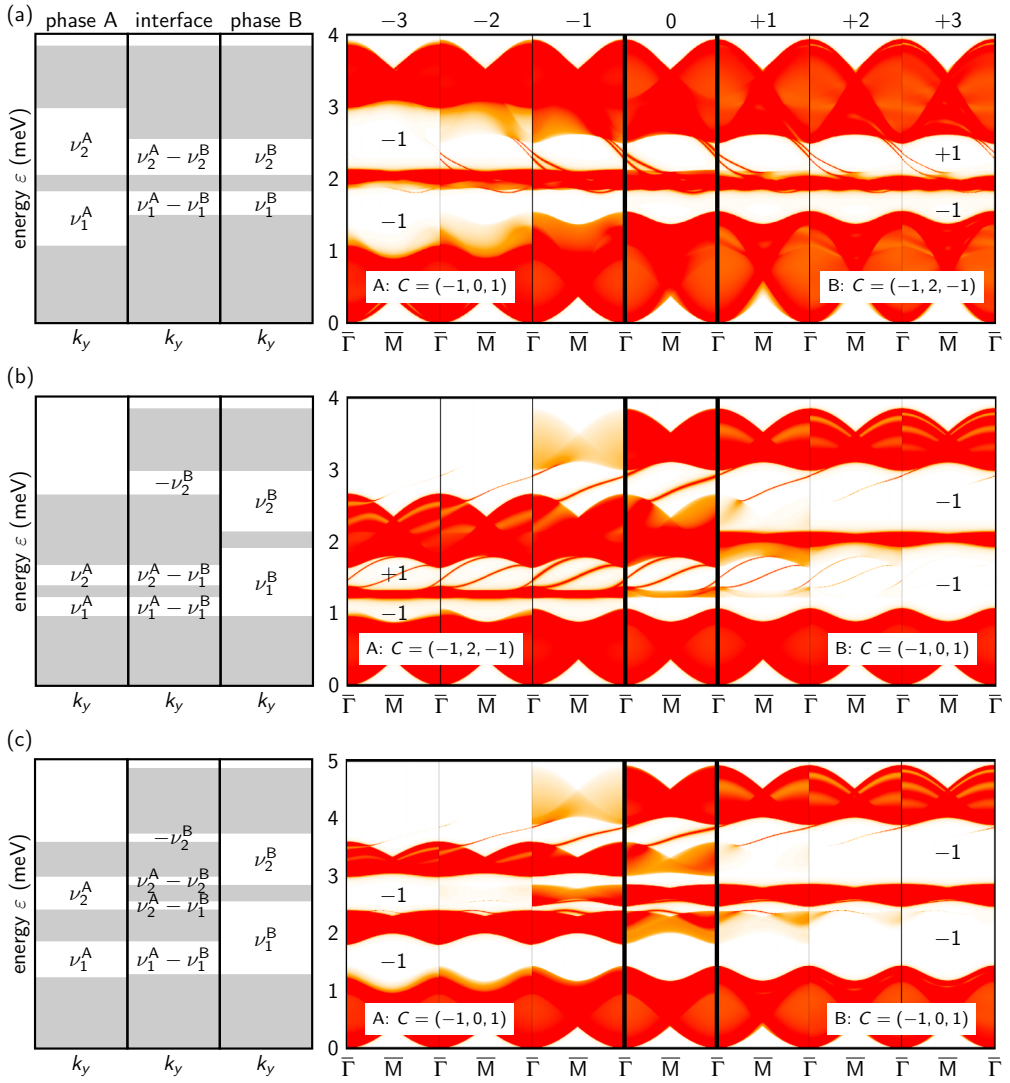

FIG. 5. (Color online) Bulk-boundary correspondence applied to magnon interface modes. (a)–(c) show three selected interface band structures that differ with respect to the number of interface band gaps and winding numbers. On the left-hand side one-dimensional magnon dispersions $\varepsilon(k_y)$ are sketched, with bulk bands in gray and winding numbers given within the band gaps. The right-hand panels display the evolution of the spectral density per principle layer (top; labeled $-3, \ldots, +3$) across the interface (layer 0). The Chern triples C of phases A and B as well as the corresponding winding numbers are indicated. Exchange parameters of A: (a) $J_{\mathrm{N}} = 2D = 1$ meV, $J_{\mathrm{NN}} = 0$ meV, (b) $J_{\mathrm{N}} = {}^{23}/_{20}D = {}^{23}/_{10}J_{\mathrm{NN}} = 0.46$ meV, and (c) $J_{\mathrm{N}} = {}^{20}/_{7}D = 1$ meV, $J_{\mathrm{NN}} = 0$ meV; B: (a) $J_{\mathrm{N}} = {}^{13}/_{7}J_{\mathrm{NN}} = {}^{13}/_{11}D = 0.65$ meV, (b) $J_{\mathrm{N}} = 2D = 1$ meV, $J_{\mathrm{NN}} = 0$ meV, and (c) $J_{\mathrm{N}} = {}^{13}/_{6}D = 1.3$ meV, $J_{\mathrm{NN}} = 0$ meV.

to the same topological phase ($\nu_i^{\mathsf{A}} = \nu_i^{\mathsf{B}}$). The right panel of Fig. 5(a) depicts the spectral density per principle layer across an interface of topologically different phases: A with Chern triple (−1,0,1) and B with (−1,2,−1). As a consequence, there is no nontrivial interface magnon within the first interface band gap [$\nu_1^{\mathsf{I}} = \nu_1^{\mathsf{A}} - \nu_1^{\mathsf{B}} = (-1) - (-1) = 0$], but the second interface band gap hosts two interface magnons [$\nu_2^{\mathsf{I}} = \nu_2^{\mathsf{A}} - \nu_2^{\mathsf{B}} = (-1) - (+1) = -2$], both with negative velocity; their spectral weights decay toward the bulk regions, which is evident from the fading color.

The exemplary dispersion of Fig. 5(b) reproduces that of Figs. 3 and 4, whose formation has been discussed in Sec. III A. This configuration hosts interface magnons even for topologically identical phases, which is readily explained by the topmost interface band gap: its winding number equals $\nu_2^{\mathsf{B}} = -1$.

The configuration sketched in Fig. 5(c) shows the maximum number of $M = 4$ interface band gaps. As an example we chose topologically identical phases with Chern triple (−1,0,1), a particularly interesting phase because all of its winding numbers are identical, that is, −1. Hence, the winding numbers of the lower three interface band gaps vanish: $\nu_1^{\mathsf{I}} = \nu_2^{\mathsf{I}} = \nu_3^{\mathsf{I}} = \nu_1^{\mathsf{A}} - \nu_1^{\mathsf{B}} = \nu_2^{\mathsf{A}} - \nu_1^{\mathsf{B}} = \nu_2^{\mathsf{A}} - \nu_2^{\mathsf{B}} = (-1) - (-1) = 0$. Only the interface winding number of the topmost gap is nonzero, and there is a single interface magnon with positive velocity in this gap [see the right-hand side of Fig. 5(c)]. Furthermore, there are two trivial interface magnons showing up within the second interface gap; they are easily identified because they do not bridge the band gap.

For completeness, other generic band structures are sketched in Fig. 6. One may think of and may discuss even more generic interface magnon dispersions. However, these

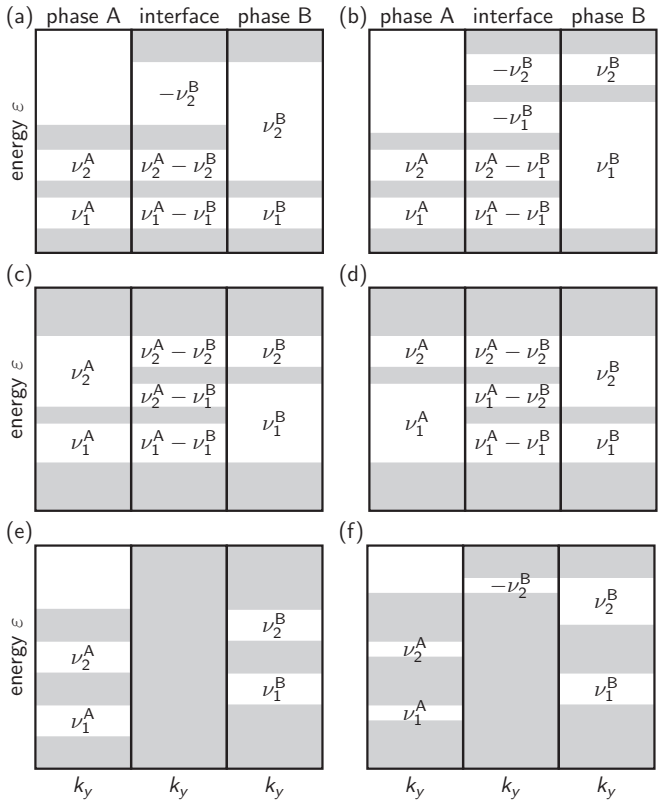

FIG. 6. Bulk-boundary correspondence of magnon interface modes. (a)–(f) display generic interface band structures with different combinations of interface band gaps and winding numbers. Bulk bands are sketched in gray; winding numbers are given within the gaps.

might be realized by unphysical combinations of exchange parameters and thus can be rendered irrelevant with respect to experiments.

The band structure shown in Fig. 6(a) is of particular interest if A and B are in the same topological phase; then the winding numbers of the lower two interface band gaps vanish, in contrast to Fig. 5(b), in which the second interface band gap may possess a nonzero winding number.

An exceptional case is given in Fig. 6(b), which displays the maximum of four band gaps: by construction, the entire magnon band width of phase A is located within the lowest band gap of B. For all topological kagome phases shown in the phase diagram (Fig. 2) there are interface magnons within the upper two band gaps of the interface dispersion since both ν_1^{B} and ν_2^{B} are nonzero.

At first glance, Figure 6(c) looks like a mirror image of Fig. 6(d); however, they are topologically different. This is due to the interface winding number of the second interface gap. Choosing an interface of topologically identical phases results in topological interface magnons within this gap as long as the two winding numbers of said topological phase differ ($\nu_1 \neq \nu_2$).

Figure 6(e) presents the case without interface gaps and therefore without topological interface magnons regardless of the topological phases of A and B. In contrast, the magnon dispersion in Fig. 6(f) has at least one interface band gap; this gap possesses a nonzero winding number for all topological kagome phases shown in Fig. 2.

IV. OUTLOOK

Because topological interface magnons transport heat (and spin) unidirectionally and are confined to a few-nanometer-wide strip along the interface, one could construct strongly confined magnon waveguides [33]. Therefore, it is desirable to identify materials whose common interface hosts nontrivial interface magnons with a single propagation direction in order to maximize the net current. Our study provides recipes for combining materials with different magnon dispersions to achieve the desired effect. We recall that even interfaces made of materials that are within the same topological phase can host nontrivial interface magnons; these could be realized by band engineering based on alloying.

To come closer to real materials, we note that the organometallic magnet Cu(1,3-benzenedicarboxylate) provides structurally perfect stacked kagome lattices built up by the Cu atoms [34]. Below 1.77 K the nearly noninteracting planes host ferromagnetic order with an intraplane interaction ratio of $\frac{D}{J_N} = 15\,\%$ ($D = \boldsymbol{D} \cdot \hat{\boldsymbol{z}}$) [35]. If the next-nearest-neighbor interaction is small, the system belongs to the topological phase $(-1,0,+1)$ (see Fig. 2) and hosts two topological edge modes propagating in the same direction. Other representatives of this crystal family might have similar properties, thus allowing for the formation of topological interface magnons at junctions.

For the future, detailed *ab initio* calculations or inelastic neutron scattering experiments are inevitable. From these, one can determine the exchange parameters and topological phases of topological magnon insulators, to name a few, the pyrochlore oxides $Lu_2V_2O_7$ (for neutron scattering experiments, see Ref. [36]), $Ho_2V_2O_7$, and $In_2Mn_2O_7$, all of which show the magnon Hall effect [37]. $In_2Mn_2O_7$ is believed to belong to a different topological phase than the other two pyrochlores because its thermal Hall conductivity has opposite sign. Thus, there is a great possibility of finding topological interface magnons at a junction of $In_2Mn_2O_7$ and one of the other two representatives.

As the topological edge magnons are still awaiting their direct experimental detection, for example, by spin-polarized electron-energy-loss spectroscopy [38] or time-resolved spectroscopies [39], we propose an indirect proof performing a "pump and probe" experiment. Given an interface with topological magnons, local heating at the interface by a laser will excite not only the isotropic bulk magnons but also said topological modes. If the two systems are chosen such that the topological interface magnons are propagating in the same direction [as, for example, in Fig. 5(b)], a deformed thermographic profile is expected. This deformation can be estimated by the ratio of the longitudinal and transverse thermal conductivities $\frac{\kappa_{xy}}{\kappa_{xx}}$, i.e., the thermal Hall angle, which is of the order of 10^{-3} for $Lu_2V_2O_7$ (Ref. [14]).

ACKNOWLEDGMENTS

This work is supported by SPP 1538 and SPP 1666 of Deutsche Forschungsgemeinschaft (DFG).

[1] H. Hasan and C. Kane, Rev. Mod. Phys. **82**, 3045 (2010).
[2] X.-L. Qi and S.-C. Zhang, Rev. Mod. Phys. **83**, 1057 (2011).
[3] M. Z. Hasan and J. E. Moore, Annu. Rev. Condens. Matter Phys. **2**, 55 (2011).
[4] Y. Hatsugai, Phys. Rev. Lett. **71**, 3697 (1993).
[5] Y. Hatsugai, Phys. Rev. B **48**, 11851 (1993).
[6] M. V. Berry, Proc. R. Soc. London, Ser. A **392**, 45 (1984).
[7] D. Xiao, M.-C. Chang, and Q. Niu, Rev. Mod. Phys. **82**, 1959 (2010).
[8] C. Strohm, G. L. J. A. Rikken, and P. Wyder, Phys. Rev. Lett. **95**, 155901 (2005).
[9] L. Zhang, J. Ren, J.-S. Wang, and B. Li, Phys. Rev. Lett. **105**, 225901 (2010).
[10] L. Zhang, J. Ren, J.-S. Wang, and B. Li, J. Phys.: Condens. Matter **23**, 305402 (2011).
[11] R. Matsumoto and S. Murakami, Phys. Rev. Lett. **106**, 197202 (2011).
[12] R. Matsumoto and S. Murakami, Phys. Rev. B **84**, 184406 (2011).
[13] L. Zhang, J. Ren, J.-S. Wang, and B. Li, Phys. Rev. B **87**, 144101 (2013).
[14] Y. Onose, T. Ideue, H. Katsura, Y. Shiomi, N. Nagaosa, and Y. Tokura, Science **329**, 297 (2010).
[15] I. Dzyaloshinsky, J. Phys. Chem. Sol. **4**, 241 (1958).
[16] T. Moriya, Phys. Rev. **120**, 1 (1960).
[17] There also exist "topological magnonic crystals" that provide topological edge modes for magnetostatic spin waves brought about by the dipolar interaction [40,41].
[18] A. Mook, J. Henk, and I. Mertig, Phys. Rev. B **89**, 134409 (2014).
[19] A. Mook, J. Henk, and I. Mertig, Phys. Rev. B **90**, 024412 (2014).
[20] W. Heisenberg, Z. Phys. **49**, 619 (1928).
[21] T. Holstein and H. Primakoff, Phys. Rev. **58**, 1098 (1940).
[22] W. Nolting and A. Ramakanth, *Quantum Theory of Magnetism* (Springer, Berlin, 2009).
[23] M. Elhajal, B. Canals, and C. Lacroix, Phys. Rev. B **66**, 014422 (2002).
[24] M. Pregelj, O. Zaharko, A. Günther, A. Loidl, V. Tsurkan, and S. Guerrero, Phys. Rev. B **86**, 144409 (2012).
[25] I. Rousochatzakis, J. Richter, R. Zinke, and A. A. Tsirlin, Phys. Rev. B **91**, 024416 (2015).
[26] M. Ramazanoglu, C. P. Adams, J. P. Clancy, A. J. Berlinsky, Z. Yamani, R. Szymczak, H. Szymczak, J. Fink-Finowicki, and B. D. Gaulin, Phys. Rev. B **79**, 024417 (2009).
[27] H. Katsura, N. Nagaosa, and P. A. Lee, Phys. Rev. Lett. **104**, 066403 (2010).
[28] F. D. M. Haldane, Phys. Rev. Lett. **61**, 2015 (1988).
[29] R. Takahashi and S. Murakami, Phys. Rev. Lett. **107**, 166805 (2011).
[30] J. Henk and W. Schattke, Comput. Phys. Commun. **77**, 69 (1993).
[31] A. Bödicker, W. Schattke, J. Henk, and R. Feder, J. Phys.: Condens. Matter **6**, 1927 (1994).
[32] See Refs. [19,42] for an application to topological magnon edge states and topological interface states between electronic topological insulators, respectively.
[33] A. Mook, J. Henk, and I. Mertig, Phys. Rev. B **91**, 174409 (2015).
[34] E. A. Nytko, J. S. Helton, P. Müller, and D. G. Nocera, J. Am. Chem. Soc. **130**, 2922 (2008).
[35] R. M. D. Chisnell, Ph.D. thesis, MIT, 2014.
[36] M. Mena, R. S. Perry, T. G. Perring, M. D. Le, S. Guerrero, M. Storni, D. T. Adroja, Ch. Rüegg, and D. F. McMorrow, Phys. Rev. Lett. **113**, 047202 (2014).
[37] T. Ideue, Y. Onose, H. Katsura, Y. Shiomi, S. Ishiwata, N. Nagaosa, and Y. Tokura, Phys. Rev. B **85**, 134411 (2012).
[38] K. Zakeri, Y. Zhang, T.-H. Chuang, and J. Kirschner, Phys. Rev. Lett. **108**, 197205 (2012).
[39] S. O. Demokritov and B. Hillebrands, in *Spin Dynamics in Confined Magnetic Structures*, edited by B. Hillebrands and K. Ounadjela, Topics in Applied Physics (Springer, Berlin, 2002), Chap. 3, p. 65.
[40] R. Shindou, R. Matsumoto, S. Murakami, and J.-i. Ohe, Phys. Rev. B **87**, 174427 (2013).
[41] R. Shindou, J.-i. Ohe, R. Matsumoto, S. Murakami, and E. Saitoh, Phys. Rev. B **87**, 174402 (2013).
[42] T. Rauch, M. Flieger, J. Henk, and I. Mertig, Phys. Rev. B **88**, 245120 (2013).